

RADIAL DISK HEATING BY MORE THAN ONE SPIRAL DENSITY WAVE

I. MINCHEV AND A. C. QUILLEN

(Department of Physics and Astronomy, University of Rochester)

Draft version July 9, 2018

ABSTRACT

We consider a differentially rotating, 2D stellar disk perturbed by two steady state spiral density waves moving at different pattern speeds. Our investigation is based on direct numerical integration of initially circular test-particle orbits. We examine a range of spiral strengths and spiral speeds and show that stars in this time dependent gravitational field can be heated (their random motions increased). This is particularly noticeable in the simultaneous propagation of a 2-armed spiral density wave near the corotation resonance (CR), and a weak 4-armed one near the inner and outer 4:1 Lindblad resonances. In simulations with 2 spiral waves moving at different pattern speeds we find: (1) the variance of the radial velocity, σ_R^2 , exceeds the sum of the variances measured from simulations with each individual pattern; (2) σ_R^2 can grow with time throughout the entire simulation; (3) σ_R^2 is increased over a wider range of radii compared to that seen with one spiral pattern; (4) particles diffuse radially in real space whereas they don't when only one spiral density wave is present. Near the CR with the stronger, 2-armed pattern, test particles are observed to migrate radially. These effects take place at or near resonances of both spirals so we interpret them as the result of stochastic motions. This provides a possible new mechanism for increasing the stellar velocity dispersion in galactic disks. If multiple spiral patterns are present in the Galaxy we predict that there should be large variations in the stellar velocity dispersion as a function of radius.

Subject headings: stellar dynamics

1. INTRODUCTION

The observed correlation between the ages and velocity dispersions of solar neighborhood stars (Eggen et al. 1962; Dennis 1966; Wielen 1977) has been a subject of study since the work of Spitzer & Schwarzschild (1951, 1953). They established that scattering of stars from initially circular orbits into more eccentric and inclined orbits was a likely explanation for the increase in velocity dispersion, σ , with age t . They suggested that massive gas clouds (then undetected) were responsible. Molecular clouds were thought to be the sole scattering agents (e.g., Mihalas & Binney 1981) until Lacey (1984) showed that the observed ratio of the dispersion in the direction perpendicular to the Galactic plane and that toward the Galactic center, σ_z/σ_R , was too low to be consistent with the predictions from this scattering process. There was also a discrepancy between the predicted and then measured relation between σ and t : if $\sigma \propto t^\alpha$, models predicted $\alpha \sim 0.20$, while observations of the time yielded $\alpha \sim 0.5$ (Wielen 1977). This resulted in the development of models that incorporated the heating of the stellar disk from transient spiral structure (Barbanis & Woltjer 1967; Sellwood & Carlberg 1984; Carlberg & Sellwood 1985) in addition to scattering from molecular clouds (Jenkins & Binney 1990; Jenkins 1992). Other proposed models for the heating of stars include scattering by halo black holes (Lacey & Ostriker 1985) or dark clusters (Carr & Lacey 1987), giant molecular clouds and halo black holes (Hänninen & Flynn 2002, 2004), and infall of satellite galaxies (Velazquez et al. 1999).

We define a steady state spiral pattern to be a spiral perturbation moving at a constant angular velocity with a fixed amplitude and a fixed pitch angle. An individual steady state spiral arm pattern is not expected to increase the velocity dispersion of a stellar

population (e.g., Binney & Tremaine 1987), though this may be violated at resonances (e.g., Contopoulos 1981; Combes et al. 1990; Fux 2001). Consequently, models used to explain the age/dispersion relation rely on transient spiral structure. In the solar neighborhood, at a distance of 8 kpc from the Galactic center and with an angular rotation speed of 220 km/s one rotation period for a star corresponds to about 0.25 Gyrs. Thus, only about 40 rotation periods have taken place during the lifetime of the Milky Way disk. Because of the small number of periods, it is difficult to apply a diffusive theory to the problem of disk heating.

Quillen (2003) pointed out that when perturbations at two pattern speeds, such as a bar and a spiral density wave are present in the disk, the stellar dynamics can be stochastic, particularly near resonances associated with one of the patterns. While this paper focused on spiral structure near the Galactic bar's outer Lindblad resonance, here we consider the more general possibility that there could be more than one wave present in the disk. There is also observational evidence for this in other galaxies, such as asymmetries in the spiral structure (e.g., Henry et al. 2003). By expanding galaxy images in Fourier components, Elmegreen et al. (1992) noted that many galaxies exhibit hidden three armed components and suggested that multiple spiral density waves can propagate simultaneously in galaxy disks. Rix & Rieke (1993), in their Fourier expansion of the near-infrared images of M51 saw both $m = 1$ and $m = 3$ components as well as the dominant 2-armed structure. In their recent work Naoz & Shaviv (2005) found evidence for multiple spiral patterns in our home galaxy. By studying the nearby spiral arms they find that the Sagittarius-Carina arm is a superposition of two features, moving at different pattern speeds. Clumps con-

taining old stars in the Solar neighborhood velocity distribution (Dehnen 1998), may be interpreted in terms of multiple stellar density waves traveling in our vicinity in the Milky Way disk (De Simone et al. 2004). Theoretically this situation corresponds to scenarios that include multiple and transient spiral density waves (e.g., Toomre 1981; Fuchs 2001) rather than those that focus on a single dominant quasi-steady mode (e.g., Lowe et al. 1994).

In this paper we are interested in the effect on the radial velocity dispersion and on the orbits of stars caused by the simultaneous propagation of two steady state spiral patterns in a combination of (strong) 2-armed + (weak) 4-armed, where the second pattern moves at an angular speed different than the first one. This situation has been motivated by Lepine et al. (2001), Drimmel & Spergel (2001), Naoz & Shaviv (2005), and Quillen & Minchev (2005) where a combination of 2-armed and a 4-armed spiral waves has been considered in the Solar Neighborhood.

We study the kinematic and spatial evolution of stars in a 2D disk by following the trajectories of non-self-gravitating particles under the gravitational potential of the background (disk and halo) and the 2 spiral density waves just described. We explore a range of pattern speed combinations and look for an increase in the radial velocity dispersion of particles.

Our simulation model is described in §2. We describe our simulations in §3-§5. A summary and discussion follows in §6.

2. NUMERICAL MODEL

2.0.1. Notation and units used

For simplicity we work in units in which the galactocentric distance to the annulus in which stars are distributed is $R_0 = 1$, the circular velocity at R_0 is $V_0 = 1$, and the angular velocity of stars is $\Omega_0 = V_0/R_0 = 1$. Actually, since we assume a flat rotation curve throughout the paper the initial circular velocity is $V_0 = 1$ everywhere. One orbital period is $2\pi R_0/\Omega_0 = 2\pi$. In our code time is in units of $1/\Omega$ whereas in the figures it is given in units of orbital periods at R_0 . The velocity vector of a star is (u, v) , where u, v are the radial and tangential velocities in a reference frame rotating with V_0 . Consequently, the tangential velocity of a star in an inertial reference frame is $V_0 + v$.

In the definitions that follow the subscript a refers to the primary, 2-armed spiral wave; similarly the subscript b refers to the secondary, 4-armed one. The azimuthal wavenumbers of each spiral wave, m_a, m_b , are integers corresponding to the number of arms. The amplitudes of the spiral wave gravitational potential perturbations are denoted as ϵ_a, ϵ_b . The spiral pattern frequencies of each spiral wave are $\Omega_{s,a}$ and $\Omega_{s,b}$. The parameters α_a, α_b are related to the pitch angles of the spiral waves, p_a, p_b , as $\alpha = m \cot(p)$, negative for trailing spirals with rotation counterclockwise. In this paper we only consider trailing spiral waves.

We write the Hamiltonian of a star as $H = H_0 + H_1$ where H_0 is the unperturbed, axisymmetric part and H_1 is a small perturbation due to the 2-armed, 4-armed, or both spiral waves. We write $H_1 = \Phi_a + \Phi_b$ where Φ_a, Φ_b are the gravitational potential perturbations due to each pattern (see next section).

In general we refer to the radial velocity dispersion as

σ_R . However, we also define 3 other symbols referring to the type of perturber we use in the Hamiltonian. Considering the above described form of H_1 , if $\Phi_a = 0$ then $\sigma_R \rightarrow \sigma_{R,b}$ (only 4-armed pattern present); if $\Phi_b = 0$, $\sigma_R \rightarrow \sigma_{R,a}$ (only 2-armed pattern present); finally, if both $\Phi_a, \Phi_b \neq 0$ then $\sigma_R \rightarrow \sigma_{R,ab}$ (both spiral waves present).

2.1. Equations of motion

We consider the 2D motion of a test particle in the mid-plane of a galaxy in an inertial reference frame. In plane polar coordinates, R, ϕ , the Hamiltonian of a star can be written as

$$H(R, \phi, p_R, p_\phi, t) = H_0(R, p_R, p_\phi) + H_1(R, \phi, t) \quad (1)$$

The first term on the right hand side is the unperturbed axisymmetric Hamiltonian

$$H_0(R, p_R, p_\phi) = \frac{p_R^2}{2} + \frac{p_\phi^2}{2R^2} + \Phi_0(R) \quad (2)$$

where we assume the axisymmetric background potential due to the disk and halo has the form $\Phi_0(R) = V_0 \log(R)$, corresponding to a flat rotation curve. Energy and angular momentum for H_0 are conserved.

In the case of one periodic perturbation there is still a conserved quantity in the reference frame rotating with the pattern. That is the Jacobi integral, $J = E - L\Omega_s$, where E is the energy of the particle, L is its angular momentum, and Ω_s is the pattern angular velocity. However, upon adding a second spiral density perturbation H does not admit any isolating integrals.

The perturbation is $H_1(R, \phi, t) = \Phi_a(R, \phi, t) + \Phi_b(R, \phi, t)$ where the 2 terms on the right hand side are the gravitational potentials due to each spiral wave. We define the subscripts a, b to denote the 2- and 4-armed spiral patterns, respectively. The perturbations are discussed in the next subsection.

Hamilton's equations applied to Eq. 1 give us the equations of motion

$$\dot{p}_R = \frac{p_\phi^2}{R^3} - \Phi'_0 - \Phi'_a - \Phi'_b \quad (3)$$

$$\dot{p}_\phi = -\frac{\partial \Phi_a}{\partial \phi} - \frac{\partial \Phi_b}{\partial \phi} \quad (4)$$

In the first of these equations the primes denote partial derivatives with respect to R .

2.1.1. Perturbation from spiral structure

We treat the spiral patterns as small perturbations to the axisymmetric model of the galaxy by viewing them as quasi-steady density waves in accordance with the Lin-Shu hypothesis (Lin et al. 1969). Each spiral wave gravitational potential perturbation is expanded in Fourier components as

$$\Phi(R, \phi, t) = \sum_m \epsilon_m \exp[i(\alpha \ln R - m(\phi - \Omega_s t - \phi_m))] \quad (5)$$

and its corresponding surface density is

$$\Sigma(R, \phi, t) = \sum_m \Sigma_m \exp[i(\alpha \ln R - m(\phi - \Omega_s t - \phi_m))] \quad (6)$$

We assume that the amplitudes, ϵ_m, Σ_m , and the pitch angles are nearly constant with radius. The strongest term for a 2-armed spiral is the $m = 2$ term and similarly $m = 4$ for a 4-armed structure. Thus only the terms corresponding to those m values are retained. In this paper we only consider 2- and 4-armed spiral waves, thus in our notation $m_a = 2$ and $m_b = 4$. Upon taking the real parts of Eqs. 5 and 6 the perturbation due to the 2-armed spiral density wave becomes

$$\Phi_a(R, \phi, t) = \epsilon_a \cos(\alpha_a \ln R - m_a(\phi - \Omega_{s,a}t - \phi_{0,a})). \quad (7)$$

Changing the subscript a to b in the above equation gives the 4-armed perturbation. The direction of rotation is with increasing ϕ and $\alpha_a, \alpha_b < 0$ ensure that each pattern is trailing.

The recent study of Vallée (2005) provides a good summary of the many studies which have used observations to map the Milky Way disk. Cepheid, HI, CO and far-infrared observations suggest that the Milky Way disk contains a 4-armed tightly wound structure, whereas Drimmel & Spergel (2001) have shown that the near-infrared observations are consistent with a dominant 2-armed structure. The dominant 2-armed and weaker 4-armed structure was previously proposed by Amaral & Lepine (1997). We adopt the same configuration in our model - a primary 2-armed and a weaker 4-armed spiral wave perturbations. What is different and new in our model is the assumption that there is a non-zero relative angular velocity between the 2 spiral patterns. This introduces an additional parameter - the pattern speed of the secondary spiral wave.

In general, an individual stellar orbit is affected by the entire galaxy. However, if tight winding of spiral arms is assumed only local gravitational forces need be considered. Ma et al. (2000) find kR for several spiral galaxies of various Hubble types to be > 6 , thus the tight-winding, or WKB approximation, is often appropriate. In the above expression k is the wave-vector and R is the radial distance from the Galactic Center (GC), related to the pitch angle p through $\cot(p) = |kR/m|$. This gives α in terms of k as $\alpha \approx |kR|$. In the WKB approximation the amplitude of the potential perturbation Fourier component is related to the density perturbations in the following way

$$\epsilon_a \sim \frac{-2\pi G \Sigma_0 S_a R_0}{|\alpha_a| V_0^2} \quad (8)$$

(Binney & Tremaine 1987). The above equation is in units of V_0^2 . Σ_a is the amplitude of the primary, 2-armed-spiral-wave mass surface density and $S_a \approx \Sigma_a/\Sigma_0$. A similar relation holds for the second spiral pattern.

2.1.2. Resonances

Of particular interest to us are the values of Ω_s which place the spiral waves near resonances. The Corotation Resonances (CR) occurs when the angular rotation rate of stars equals that of the spiral pattern. Lindblad Resonances (LRs) occur when the frequency at which a star feels the force due to a spiral arm coincides with the star's epicyclic frequency, κ . As one moves inward or outward from the corotation circle the relative frequency at which a star encounters a spiral arm increases. There

are 2 values of R for which this frequency is the same as the epicyclic frequency and this is where the Outer Lindblad Resonance (OLR) and the Inner Lindblad Resonance (ILR) are located.

Quantitatively, LRs occur when $\Omega_s = \Omega_0 \pm \kappa/m$. The negative sign corresponds to the ILR and the positive - to the OLR. Specifically, assuming a flat rotation curve, for the 4:1 ILR $\Omega_s = 0.65\Omega_0$, for the 4:1 OLR $\Omega_s = 1.35\Omega_0$, for the 2:1 ILR $\Omega_s = 0.3\Omega_0$, and for the 2:1 OLR $\Omega_s = 1.7\Omega_0$. Corotation of each spiral pattern occurs at $\Omega_s = \Omega_0$.

2.2. Simulation method

To investigate the effect of a second spiral density wave on the orbits of stars, we ran simulations of test particles in a disk with two spiral density waves. As done by De Simone et al. (2004) the amplitude of each wave was varied, however the pitch angle and pattern speed were held fixed during the integrations. We are restricting this initial study to this type of spiral arm growth (no swing amplifier mechanism).

2.2.1. Initial conditions

Positions of test particles (stars) were chosen randomly with a uniform density distribution in both radial and azimuthal directions. Thus, we distribute stars in an annulus of an inner and outer radii $R_0 - \Delta R, R_0 + \Delta R$, where for most of the runs ΔR is 0.3. All stars were given the same initial velocity $(u, v) = (0, 0)$ consistent with a flat rotation curve and an initially cold stellar disk.

We now describe the growth of the spiral density waves. The amplitudes, ϵ_a, ϵ_b are zero before t_0 , grow linearly with time at $0 < t < t_1$ and stay constant at $\epsilon_a = \epsilon_{max,a}$, $\epsilon_b = \epsilon_{max,b}$ after $t = t_1 = 4$ rotation periods.

Simulations were run for 40 rotation periods, which corresponds to about 10 Gyr. Heating rates were estimated calculating the radial velocity dispersion (the standard deviation of the radial velocity component u), every rotational period. This was done for all stars in the annulus $(R_0 - \Delta R, R_0 + \Delta R)$ where $\Delta R = 0.05$.

The standard deviation was computed as the square root of the bias-corrected variance:

$$\sigma_R = \sqrt{\frac{\sum_{i=1}^n (u_i - \bar{u})^2}{n-1}} \quad (9)$$

where n is the number of stars in the bin (the annulus of width $\Delta R = 0.05$ centered on R_0 , described above) and $\bar{u} = (\sum_{i=1}^n u_i)/n$. Table 1 shows the parameters for which simulations were run.

2.2.2. Numerical accuracy

Calculations were performed in double precision. We checked how energy was conserved in an unperturbed test run. The initial energy was compared to that calculated after 40 periods (≈ 10 Gyr) and the relative error was found to be $|\Delta E/E(0)| < 8.48 \times 10^{-14}$. We also checked the conservation of the Jacobi integral J in the presence of one periodic perturbation. The relative error found in this case was $|\Delta J/J(0)| < 3.11 \times 10^{-12}$.

3. ONE SPIRAL PATTERN

To tell the difference between the effect of one spiral pattern and both patterns, we first ran comparison simulations with only one spiral pattern present. In each run we integrated 6000 particles. Parameters used for integrations are listed in Table 1.

In Fig.1 we plot the radial velocity dispersion, $\sigma_{R,a}$ as a function of time for the primary 2-armed spiral wave only. In all panels the amplitude of the gravitational perturbation is kept fixed at $\epsilon_a = -0.006$ once the wave is grown, and the pitch angle function is $\alpha_a = -6$ which corresponds to $p_a \approx -18^\circ$. Each panel in Fig. 1 shows the increase of the radial velocity dispersion with time at a different pattern speed, $\Omega_{s,a}$.

Logarithmic spirals are known to be self-similar. Due to this fact, changing the angular frequencies of the spiral waves is equivalent to changing the radius. Since we assumed a flat rotation curve, $V_0 = 1$ everywhere and the angular velocity of stars varies with radius as $\Omega = V_0/R = 1/R$. On the other hand, since the pattern speed, Ω_s does not vary with R , i.e., the pitch angle is constant, a spiral rotates as a rigid body. It follows that in the units used in this paper we can just substitute R for $\Omega_{s,a}$ in Fig. 1, placing R_0 at $\Omega_{s,a} = 1.0$. We note that since stars in the inner parts of a flat-rotation-curve galaxy complete one rotation period faster than stars in the outer parts, 40 rotation periods at R_0 translates as a larger number of revolutions in the inner parts and a smaller number in the outer parts. Assuming a corotation radius near R_0 and a galactic radius of $\sim 2R_0$, Fig. 1 gives the heating as a function of radius in the galaxy for one pattern. The top left hand panel shows pattern speeds placing R_0 near the 2:1 ILR. The lower right hand panel shows pattern speeds placing R_0 near the 2:1 OLR.

As the spiral amplitude, ϵ_a , reaches its maximum value the radial velocity dispersion levels off. As predicted by many previous theoretical investigations, there is no heating after the wave is grown. As expected, large radial velocity dispersion values are found only near the 2:1 Lindblad resonances ($\Omega_{s,a} = 0.3, 1.7$). This is consistent with Lynden-Bell & Kalnajs (1972) who showed that steady spirals heat stars only at the Lindblad resonances. Note that at and around corotation ($\Omega_{s,a} = 1.0$) random motions of stars were not increased.

The effect of a weak 4-armed spiral pattern on the radial velocity dispersion of stars is shown in Fig. 2 for 3 values of the gravitational potential perturbation amplitude, ϵ_b . Different line styles show $\epsilon_b = -0.001$ (dotted), $\epsilon_b = -0.002$ (dashed), and $\epsilon_b = -0.003$ (solid). As in the case of the 2-armed spiral wave, relatively large $\sigma_{R,b}$ values are observed only near the first order, 4:1 LR ($\Omega_{s,b} = 0.65, 1.35$). Substituting R for $\Omega_{s,b}$ in Fig. 2 gives $\sigma_R = \sigma_R(R)$ in the range ($R = 0.5, R = 1.6$).

In both the 2- and 4-armed spiral structures the initial rapid increase ends when the spiral amplitudes attain their maximum values ($t \approx 4$ rotations) and are fixed for the rest of the runs. This observation will later be contrasted with the effect of the simultaneous propagation of 2 spiral waves (see §4.2).

4. TWO SPIRAL PATTERNS GROWN SIMULTANEOUSLY

We next ran simulations with two spiral density waves moving at different pattern speeds. The spiral amplitudes were grown simultaneously over 4 rotation periods as in the case of only one spiral wave.

4.1. Heating in $(\Omega_{s,a}, \Omega_{s,b})$ -space

First we carried out a set of integrations with 1000 particles going through all the possible combinations of the two pattern speeds in the range (0.1,2.0) for the $\Omega_{s,a}$ and (1.5,1.6) for $\Omega_{s,b}$, in steps of 0.1, and in units of the angular rotation rate, Ω_0 at R_0 . The chosen ranges of $\Omega_{s,a}$ and $\Omega_{s,b}$ ensure that we cover the Lindblad and corotation resonances of each spiral wave. The results are shown as the $(\Omega_{s,a}, \Omega_{s,b})$ -space contour plots in Figures 3 and 4, described below.

Horizontal axis is $\Omega_{s,a}$ and vertical axis is $\Omega_{s,b}$ for each panel. Each panel corresponds to a different secondary spiral wave amplitude, $\epsilon_b = -0.001, -0.002, -0.003$. The primary pattern amplitude is constant for all panels at $\epsilon_a = 0.6$. Spiral amplitudes were grown simultaneously in 4 rotational periods and were kept fixed after that.

In Fig. 3 contours show

$$\Delta\sigma_R \equiv \sigma_{R,ab} - \sqrt{\sigma_{R,a}^2 + \sigma_{R,b}^2}. \quad (10)$$

Here $\sigma_{R,a}$ and $\sigma_{R,b}$ are the radial velocity dispersions as a result of only the primary or only the secondary spiral patterns, respectively. These were time averaged over 40 galactic rotations, excluding the time during which wave amplitudes grew (initial 4 periods). Similarly, $\sigma_{R,ab}$ is the time average of a simulation run with both patterns perturbing the test particles. Consequently, $\Delta\sigma_R$ gives the additional heating caused by the combined effect of the two perturbers as opposed to the sum of the heating that would have been produced if each spiral wave propagated alone.

The dashed lines show the locations of corotation and Lindblad resonances due to each of the two spiral wave perturbations. Next to each dashed line we labeled the corresponding resonances by denoting the corotation resonance with "CR", and the outer and inner Lindblad resonances with "OLR" and "ILR".

Grayscale for $\Delta\sigma_R$ was normalized to the maximum value of the three panels allowing a proper comparison among the panels. Darker regions corresponds to larger values of $\Delta\sigma_R$.

We see that $\Delta\sigma_R > 0$ for most combinations of angular velocities which implies that spiral waves interfere and produce additional heating. In all the panels maximum values of $\Delta\sigma_R$ are attained mainly along the lines $\Omega_{s,a}=1.0$ and $\Omega_{s,b}=1.0$ corresponding to the CR of each spiral wave. A notable exception to this trend is the intersection of these lines where patterns do not have relative motion with respect to each other. As the absolute value of the secondary spiral wave amplitude, $|\epsilon_b|$, is increased from 0.001 to 0.003 structure in the $\Omega_{s,a}, \Omega_{s,b}$ -plane seems not to change significantly, however $\Delta\sigma_R$ is increased.

It is interesting to note the lack of heating due to the effect of the coupling between the two spiral waves at the 2:1 ILR and on the outside of the 2:1 OLR of the 2-armed spiral wave, and at the vertical line $\Omega_a \approx 0.7$ which is just outside the 4:1 ILR with the same perturbation.

We mentioned earlier that changing Ω_s and keeping R constant is equivalent to changing R and keeping Ω_s

constant. Thus, for a given set of pattern speeds, a line at 45° slope in Fig. 3 predicts the variation of $\Delta\sigma_R$ with radius, R , where the intercept of the line is set by the relative angular frequency, $\Delta\Omega_s \equiv \Omega_{s,a} - \Omega_{s,b}$. Depending on the given $\Delta\Omega_s$, a galaxy heated by two spiral density waves would exhibit different variation of the radial velocity dispersion with radius. For example, if $\Delta\Omega \approx 0$ then the galaxy would not be heated efficiently. This is expected since, as mentioned earlier, steady spirals heat stars only at the LRs. If, on the other hand, $\Delta\Omega \approx 0.3$ then the currently examined heating mechanism would prove quite efficient and would effect stars over a wide region. It is evident from the figure that heating takes place mainly near the CR and OLR of primary, and near the CR of the secondary pattern.

Similarly to the $\Delta\sigma_R$ contours shown in Fig. 3 we plot contours of the radial velocity dispersion as the result of the simultaneous propagation of the two spiral waves, $\sigma_{R,ab}$, in Fig. 4.

Here maximum values are attained at the 2:1 ILR of the primary, $\epsilon_a = -0.006$ spiral wave. We believe that in reality the 2:1 ILR is too strong to maintain spiral structure for strong spirals so we regard the results observed in this location on the $\Omega_{s,a}, \Omega_{s,b}$ -plane as unphysical. It is possible that in reality spiral amplitude decreases as this resonance is reached or that spiral arms end there. Aside from the 2:1 ILR of the 2-armed spiral wave in all the panels high values of $\sigma_{R,ab}$ are observed around the 2:1 OLR of the primary spiral wave or near resonances with the primary and the secondary pattern taking place at the same time (where dashed lines cross). As in Fig. 3 an exception to the last statement is the point ($\Omega_{s,a} = 1.0, \Omega_{s,b} = 1.0$) for which the lowest values in $\sigma_{R,ab}$ are reached. Again, this corresponds to both patterns placing stars at the CR and thus no relative motion between them.

In the following section we chose interesting points corresponding to specific combination of the pattern angular velocities in Fig. 3 and plotted the radial velocity dispersion, $\sigma_{R,ab}$, as function of time, t , to compare to the effect of the single spiral waves described in §3. Parameters for all runs can be found in Table 1.

4.2. Time evolution of the radial velocity dispersion at the CR and OLR of primary pattern

To better understand the nature of the process giving rise to the structure seen in Figures 3 and 4 we plotted the time evolution of $\sigma_{R,ab}$ and $\sqrt{\sigma_{R,a}^2 + \sigma_{R,b}^2}$ (as defined in the previous subsection, see Eq. 10). These dispersions are shown in Figures 5-7 as functions of time. We chose to consider stars near the corotation resonance with the primary pattern and with different values for the secondary pattern speed. For reference, the time average values of $\Delta\sigma_R$ and $\sigma_{R,ab}$ are given by the vertical line $\Omega_{s,a} = 1.0$ in Fig. 3 and the same line in Fig. 4, respectively.

The solid lines in Figures 5-7 depict the effect of the simultaneous propagation of a 2- and a 4-armed spiral patterns on the radial velocity dispersion, $\sigma_{R,ab}$, as a function of time, t , in units of galactic rotation periods. Figures 5, 6, and 7 differ only in the value of the amplitude of the secondary spiral wave, to wit, $\epsilon_b = -0.001, -0.002, -0.003$, respectively. The value of

the primary spiral wave amplitude is fixed for all 3 Figures with $\epsilon_a = -0.006$. The 2-armed spiral structure has the same parameters as that shown in Fig.1 for which $\Omega_{s,a} = 1.0$ (CR), whereas the 4-armed spiral wave has different angular velocity in each panel of Figures 5-7. The dispersion due to the latter perturbation alone, $\sigma_{R,b}$, was shown in Fig. 2. For comparison, in addition to $\sigma_{R,ab}$ (solid line) we also plotted $\sqrt{\sigma_{R,a}^2 + \sigma_{R,b}^2}$ (dashed line) (see Eq. 10).

The 4:1 resonances of the secondary spiral wave are seen in the lower left 2 panels (4:1 OLR) and the upper middle 2 panels (4:1 ILR). Note the big dynamical changes at those locations for the case of $\sigma_{R,ab}$:

- (1) $\sigma_{R,ab}$ increases up to a factor of ≈ 3 compared to the dispersion expected from the noninteracting spiral waves, $\sqrt{\sigma_{R,a}^2 + \sigma_{R,b}^2}$ (i.e., panels with $\Omega_b = 1.2, 1.5$, Figures 5-7);
- (2) $\sigma_{R,ab}$ grows with time. In Fig. 5 at $\Omega_{s,b} = 0.6, 0.7, 1.4$ $\sigma_{R,ab}$ increases until $t \approx 10$; for $\Omega_{s,b} = 0.8, 1.2, 1.5, 1.6$ $\sigma_{R,ab}$ increases at even later times of 20-30 periods. This does not happen when only one pattern is present.
- (3) resonances have effect over a larger range of angular velocities, compared to $\sqrt{\sigma_{R,a}^2 + \sigma_{R,b}^2}$, and thus over a larger range of radii.

As noted earlier, in the case of only one spiral density wave large effects are primarily observed near the 2:1 Lindblad resonances for the 2-armed, and near the 4:1 Lindblad resonances for the 4-armed spiral patterns during the growth of the perturbations only. In contrast, when two spiral waves at a particular combination of pattern speeds are present, $\sigma_{R,ab}$ keeps increasing even after the maximum values of the potential amplitudes, ϵ_a and ϵ_b , are reached. We expect the most likely explanation for this is that the particular combination of pattern speeds, namely, a 2-armed spiral at the CR and a 4-armed one near the ILR or OLR, creates stochastic motion due to resonance overlap. This is analogous to the bar - spiral wave overlap described by Quillen (2003), found to produce a stochastic region in the vicinity of the Galactic bar's OLR. In these conditions stars are expected to diffuse radially in real space (see §5.2).

The dispersion $\sigma_{R,ab}$ grows with time up to a specific value of t (saturation time) after which it does not increase anymore. It is interesting to note the decrease in the saturation time as the strength of the secondary spiral increases in Figures 5-7.

If the observed increase of $\sigma_{R,ab}$ with t is due to the presence of both the CR of the primary, 2-armed and the LRs of the secondary, 4-armed spiral waves, then one would expect that as one moves away from the LRs of the secondary pattern the effect on the radial dispersion would diminish. This is generally the trend observed in Figures 5-7, however on both sides of the 4:1 OLR the opposite effect is seen. At $\Omega_{s,b} = 1.2, 1.5$ large values of $\sigma_{R,ab}$ are still evident. In fact, at the points $(\Omega_{s,a}, \Omega_{s,b}, t) = (1, 1.2, 40), (1, 1.5, 40)$ in Fig. 5 the ratio $\sigma_{R,ab}/\sqrt{\sigma_{R,a}^2 + \sigma_{R,b}^2}$ attains its maximum value of ≈ 3.5 . These high values of $\Delta\sigma_R$ on each side of the 4:1 OLR of the 4-armed pattern were anticipated, considering the structure along the line $\Omega_{s,a} = 1.0$ in Fig. 3.

In Fig. 8 we plot the time evolution of $\sigma_{R,ab}$ and

$\sqrt{\sigma_{R,a}^2 + \sigma_{R,b}^2}$ for $\Omega_{s,a} = 1.7$. At this angular velocity of the primary pattern particles are placed at the 2:1 OLR. The gravitational perturbation amplitude of the secondary wave is $\epsilon_b = -0.003$; the primary one has the default value of $\epsilon_a = -0.006$. Obviously, the fraction $\sigma_{R,ab}/\sqrt{\sigma_{R,a}^2 + \sigma_{R,b}^2}$ is much smaller than that observed in Figures 5-7. This was expected in view of Figures 3 and 4.

It is clear from Figures 5-8 that the velocity dispersion in the presence of 2 patterns, $\sigma_{R,ab}$, exceeds that expected from each individual pattern $\sqrt{\sigma_{R,a}^2 + \sigma_{R,b}^2}$. Furthermore, $\sigma_{R,ab}$ continues to increase with time for some values of $\Omega_{s,a}, \Omega_{s,b}$. This contrasts with the predictions for heating due to transient spiral density waves. Additional heating occurs in the presence of 2 waves and the interplay of the 2 waves contributes to additional heating after they have ceased to grow.

We also considered the more realistic situation in which the second spiral density wave was grown at a later time than the first one. At all parameters kept the same as those used to produce Figures 5, 6, and 7, we ran simulations in which the starting time for the secondary spiral wave amplitude was set to 2, 4, 7, 15, and 20. We found that the sole effect of the delayed second spiral was to delay the starting point of the radial dispersion increase.

5. ORBITS OF STARS NEAR RESONANCES IN THE ROTATION FRAME OF THE PATTERN

To understand what causes the heating observed in Figures 5-8 we will next look at the shapes of the orbits of test particles when subjected to only one of the 2 spiral perturbations and then compare those to the orbits of particles in the presence of both.

The description of the particle trajectories below is based on movies we made for each simulation run in the current section, 5. Snaps from the movies are shown in the figures below.

5.1. Orbits of stars subjected to one spiral wave only

We offer a qualitative description of the orbits of stars near corotation with the primary spiral wave only, as seen in a reference frame rotating with the spiral pattern. To simplify this task as much as possible we integrated 1000 particles placed at different radius R and uniformly distributed azimuthally. Different panels in Fig. 9 show particles initially moving:

- (a) just inside the CR ($R = 0.9$),
- (b) exactly at the CR ($R = 1.0$), and
- (c) just outside the CR ($R = 1.1$). These panels are shown for $t = 40$ rotation periods for 3 separate simulations. Dashed circles show the initial distribution of the particles.

Just inside of the corotation circle stars are moving faster than the spiral pattern (Fig.9, a). In a reference frame rotating with the spiral, their orbits are confined, depending on the azimuthal angle of each star at the time the spiral perturbation is turned on, to one of 3 types of orbits. These are an oval orbit and two banana-shaped closed curves situated outside the initial circle, the cusps of which coincide with the two spiral arms.

Just outside of the corotation radius (Fig.9, c) stars follow similar orbits to the ones described above, except

that because the spiral wave moves faster than the stars, the "banana" orbits are situated inside both the oval-shaped orbit and the initial circle (at R_0). Furthermore, the oval orbit is flattened at a 90° phase difference compared to the same type of orbit inside of the CR.

Finally, exactly at corotation a more complicated situation is observed (Fig.9, b). As seen in the reference frame of the spiral, stars move on 2 families of nested closed curves similar to the 2 "banana" orbits discussed above. Each such orbit protrudes equally radially inward and outward. Note, that the third, oval shaped orbit is not present here. Stars which happened to be at the arms at the time the wave was turned on, stayed there and the rest are not allowed to cross an arm at any time.

We talked about the orbits of stars but what Fig. 9 actually shows are snapshots at a single time, $t = 40$ rotations. During the entire simulation a given closed contour on which stars move does not change shape or orientation as seen in the reference frame of the spiral wave. Consequently, a plot showing the orbital trajectory of a single particle would look exactly like the snapshots in these pictures. However, if a contour on which stars move *does* change shape or orientation then it cannot be regarded as the trajectory that a single star would follow.

Similarly to the CR of the 2-armed spiral wave, information about the orbits of stars placed at and near the 4:1 OLR ($\Omega_b = 1.65$) of the secondary, 4-armed spiral wave can be obtained from Fig. 10. In all panels all parameters are kept the same except for the radius at which stars were initially distributed. The pattern amplitudes are $\epsilon_b = -0.002$, $\epsilon_a = 0$ and angular velocity is $\Omega_b = 1.65$. Panels show stars initially moving on a circle of radius:

- $R = 0.9$ or just inside the 4:1 ILR (Fig. 10, a),
- $R = 1.0$ or exactly at the 4:1 ILR (Fig. 10, b), and
- $R = 1.1$ or just outside the 4:1 ILR (Fig. 10, c).

The snapshots are at time $t = 40$ galactic rotations. As we discussed at the end of the previous paragraph, the curve on which test particles lie at a point in time is not necessarily the trajectory which a single particle would follow in time (in a frame rotating with the pattern). It turns out that only Fig. 10, (b) depicts a curve which changes shape and orientation as the system develops in time. Therefore, we do not regard Fig. 10, (b) as the trajectory of a particle.

The particle trajectories (in a frame rotating with the pattern) in panels (a),(c) of Fig. 10 form as soon as the spiral wave amplitude, ϵ_b , is grown (4 galactic rotations) and do not change until the end of our runs (40 rotation periods). However, exactly at the 4:1 ILR (Fig. 10, b) the rectangular curve starts to form at $t \approx 2$ rotations with its vertices supporting the spiral structure and starts to spin clockwise in the rotation frame of the pattern. As it does so its vertices sharpen to achieve the curve seen in Fig. 10, (b). The curve goes back to being oblate as the rectangle's vertices reach the arms again. This process is repeated with a period of about 9 galactic rotations. Note that star orbits support the spiral structure outside the 4:1 ILR (Fig.10, c) but are out of phase with the perturbation inside of it (Fig.10, a). The orientation of the orbits changes at the resonance. It is known that strong 2-armed

density perturbations can excite square-shaped orbits as well (Contopoulos & Grosbol 1986; Quillen & Minchev 2005). However, in this case (secondary order in the epicyclic amplitude 4:1 ILR) the spirals are supported by star orbits interior to the 4:1 ILR and are not supported by the orbits of stars having their guiding radii exterior to it. This behavior prompted Contopoulos (1985) to propose that 2-armed spiral waves ended at the 4:1 ILR.

To complete the picture we lastly show the behavior of stars when subjected to the 4:1 OLR of the secondary, 4-armed spiral wave only. Fig. 11 shows a snapshot of the real-space particle distributions at time $t=40$ galactic rotations. Pattern speeds and gravitational potential amplitudes were the same for each panel, $\Omega_b = 1.35$ and $\epsilon_b = 0.002$, respectively. The initial distribution of each simulation was at:

$R = 0.9$ or just inside the 4:1 OLR (Fig. 10, a),
 $R = 1.0$ or exactly at the 4:1 OLR (Fig. 10, b), and
 $R = 1.1$ just outside the 4:1 OLR (Fig. 10, c).

As in Fig. 10, inside and outside the resonance the initially circular curve did not change shape or orientation, thus it represents the approximately closed orbit of stars in a frame rotating with the pattern (Fig. 10, a, c). On the other hand, Fig. 10, (b) shows a curve which spins as the system develops in time.

In all the cases but Figures 10, (b) and 11, (b), the initial circles assumed some particular shape at the end of the growth of the spiral waves and did not change for the remaining time. To check whether this was the result of an adiabatic perturbation we also tried using a sudden perturbation by growing the spiral in just 0.1 period, as opposed to the default value of 4 periods, and found similar results.

5.2. Orbits of stars subjected to 2 spiral density waves moving at different angular velocities

In this section we attempt to look for an answer to the following question: What process gives rise to the continuous increase of the radial velocity dispersion, σ_R , with time, t , in Figures 5-8?

We will only look at the following combinations of patterns:

- (i) a 2-armed spiral wave at the CR ($\Omega_{s,a} = 1.0$) propagating simultaneously with a 4-armed one just outside the 4:1 ILR ($\Omega_{s,b} = 0.7$).
- (ii) a 2-armed spiral wave at the CR ($\Omega_{s,a} = 1.0$) propagating simultaneously with a 4-armed one just inside the 4:1 OLR ($\Omega_{s,b} = 1.2$).

The sole effect of a 2-armed spiral wave, moving at a pattern speed which places stars at the CR, on the stars' orbits was shown in panel (b), Figure 9. The trajectory of a star moving exterior to the 4:1 ILR ($\Omega_{s,b} = 0.7$, considered in (i) above) is closest to the curve seen in panel (c), Fig. 10, which could be perceived as the result of a simulation with an initial spatial distribution on a circle of radius $R = 1.0$ and a pattern speed of $\Omega_{s,b} = 0.75$ (see 3-rd paragraph of §3). Similarly, the trajectory of a star moving inside the 4:1 OLR ($\Omega_{s,b} = 1.2$, considered in case (ii) above) is closest to the curve seen in panel (a), Fig. 11 which corresponds to an initial spatial distribution on a circle of radius $R = 1.0$ and a pattern speed of $\Omega_{s,b} = 1.25$.

Remember that in Figures 5-8 initially we distributed stars in the annulus $(R_0 - \Delta R, R_0 + \Delta R)$ with $\Delta R = 0.3$ and $R_0 = 1$. Trajectories of test particles were followed for 40 rotations (the lifetime of the Galaxy at R_0) and σ_R was computed every period in the annulus $(R_0 - \Delta R, R_0 + \Delta R)$ with $\Delta R = 0.05$. Because of the differential rotation of stars in the disk, the initial velocities of all test particles are fixed at $(v, u) = (V_0, 0)$ so it takes longer for particles at larger R to complete one period compared to particles at smaller R . On the other hand, spirals move as rigid bodies. It is obvious that particles moving at different radii would see the spiral structure moving at different pattern speed. Stars contributing to σ_R could have come from various radii, thus responding to different pattern-speed spiral waves. This is a complicated process. To simplify it, considering first the panel for which $\Omega_{s,b} = 0.7$ in Fig. 6 (case (i) above), we give the following illustration:

(1) One can imagine the initial spatial distribution of particles is made of rings of stars at different radii between $R_0 - \Delta R$ and $R_0 + \Delta R$. Thus one can simplify the problem by looking at rings of stars. On a particular ring all stars feel a spiral pattern moving at the same pattern speed. Furthermore, a plot of the time development of the spatial distribution of stars would be much more informative than a similar plot of a simulation run with the set up used for Fig. 6, panel with $\Omega_{s,b} = 0.7$.

(2) Integrate 3 such rings corresponding to specific radii in the initial annulus distribution of Fig. 6. We chose those to be at $R = 0.9, 1.0, 1.1$.

(3) Plot the spatial distribution of stars at different times to see whether particles, initially positioned on the circle of radius R , diffuse radially as was speculated earlier.

Plotted in Fig. 12 are 3 steps of the 40-rotation-period time evolution of 3 rings of stars at the radii chosen in step 2 above. Rows from top to bottom show particles subject to 2 pattern speeds with angular velocities $\Omega_{s,a} = 1.0$, $\Omega_{s,b} = 0.7$ (case (i) above) and initially positioned in a ring of radius:

$R = 0.9$ (Fig. 12, a),

$R = 1.0$ (Fig. 12, b), and

$R = 1.1$ (Fig. 12, c).

Snapshots are at times $t = 10, 25$, and 40 galactic rotation periods. The crosses show the position of the galactic center.

The 3 systems in Fig. 12 behave very differently compared to the ones depicted in Figures 9 and 10. Note that stars *do* diffuse radially. Orbits are not confined to narrow regions in phase space as was observed in Figures 9-11. We see very different dynamics in the trajectories of particles. In the first snap (at $t=10$) it is clear that inside the CR stars are scattered radially outward whereas the opposite effect is seen exterior to the CR. This is similar to the behavior of stars in Fig. 9 and thus must be related to the proximity of the CR. However, stars do not lie on a specific curve as in the case of only one perturbation. As one moves to panels at $t = 25, 40$ a randomization in the azimuthal direction is apparent. As was seen in Fig. 6, panel with $\Omega_{s,b} = 0.7$, saturation time was reached at around $t \approx 10$ periods. This is consistent with Fig. 12 where the real space particle distributions in the panels with $t = 25, 40$ for

each row do not appear much different. Note that, in a simplified way, the time development of the real-space distribution of stars in Fig. 6, panel with $\Omega_{s,b} = 0.7$, can be obtained by overlapping the 3 rows in Fig. 12.

Similarly to Fig. 12, radial diffusion of stars is expected in the vicinity of the CR due to the 2-armed pattern and the 4:1 OLR of the secondary, 4-armed one (case (ii) above). We show in Fig. 13 the time development of the real space particle distribution of 3 initially circular rings of stars taken from the initial annulus distribution in Fig. 6, panel with $\Omega_{s,b} = 1.2$. The primary spiral wave angular velocity is $\Omega_b = 1.0$ (as in Fig. 12) placing stars at the CR, but the secondary pattern speed is now $\Omega_b = 1.2$, which places stars just inside the 4:1 OLR. We see in Fig. 6, panel with $\Omega_{s,b} = 1.2$, that the extra velocity dispersion coming from the correlated spirals is about 3 times that due to the individual ones, i.e., $\Delta\sigma_R \approx 3$ (see Eq. 10) whereas in the $\Omega_{s,b} = 0.7$ panel of the same figure $\Delta\sigma_R \approx 2$. We consequently expect stronger effect on the radial diffusion in the case of a secondary spiral wave moving at $\Omega_{s,b} = 1.2$. This is indeed the case as Fig. 13 shows.

The effect of the addition of a second pattern at a different pattern speed than the first one is the observed radial diffusion in Figures 12 and 13. For this to work the 2 spirals must be correlated so that particles encounter each spiral wave in a systematic manner. The radial diffusion of stars is related to the increase of the radial velocity dispersion, σ_R , with time, seen in Figures 5-8. This is most prominent around the CR or the OLR of the 2-armed spiral wave and the OLR and ILR of the secondary, 4-armed one.

6. SUMMARY AND DISCUSSION

In this paper we have considered the effect of the simultaneous propagation of 2 spiral density waves moving at different pattern speeds, on the stellar radial velocity dispersion, σ_R of a galactic disc. The numerical experiments performed concentrated on a primary 2-armed spiral wave and a weaker 4-armed one and their effect on the orbits of particles initially placed into circular orbits. This choice of spiral structure is motivated by recent COBE observations (Drimmel & Spergel 2001).

Following the growth of the spiral density waves, we find that the variance of the radial velocity resulting from 2 spiral waves exceeds that expected from the sum of the variances from each pattern. In other words, the velocity dispersion in an integration with both spiral density waves is larger than the sum of the effects of the individual spiral density waves. The increase in σ_R is particularly prominent at and near a corotation resonance with a primary, 2-armed spiral wave, in a combination with a secondary, 4-armed one at and near the OLR and ILR. Furthermore, we find that σ_R continues to increase near these resonances even after the spiral density waves have ceased to grow. This suggests that the coupling between the 2 spiral waves causes particles to diffuse in real space, even though the spiral density wave amplitudes are held

fixed.

We have examined the distribution of stars perturbed by one and two spiral density waves. When only one spiral density wave is present, little diffusion in phase space occurs. A comparison between these distributions (see Figures 9-13) shows that diffusion is observed when multiple waves are present. This comparison confirms our hypothesis that the combined effect of the two spiral density waves causes stochastic diffusion of stars in phase space.

Previously studied heating mechanisms have concentrated on heating from transient spiral density waves (e.g., Sellwood & Carlberg 1984; Carlberg & Sellwood 1985; De Simone et al. 2004; Jenkins & Binney 1990; Sellwood & Binney 2002). However in that case changes in the stellar velocity dispersion only occur during the growth or decay of spiral density waves. Here we observe an increase in the velocity dispersion even when the spiral density waves have ceased to grow. Hence, this is a different heating mechanism compared to those explored by these previous investigations. The heating we see here is similar to that observed at resonances in barred galaxies. For example, Combes et al. (1990) observed stochastic heating in 3D simulations of barred peanut galaxies. We suggest that stochastic heating could also occur in disks of galaxies if more than one spiral density wave is present. In this case we could consider the source of the stochastic behavior the overlap of the two resonant perturbations (e.g., Murray & Holman 1999; Lecar et al. 2001).

We have established the possible combinations of pattern speeds for which heating is significant. This heating mechanism is strongly dependent on the relative velocity between stars and the spiral pattern and thus on the galactocentric distance, R (e.g., see Figures 3,4). Consequently we expect strong variations in the velocity dispersion as a function of position in the Galaxy.

Future work could consider the role of Giant Molecular Clouds (GMC) in addition to the currently explored mechanism by carrying out simulations in 3 dimensions. Here we have considered spiral density waves with fixed amplitudes and pitch angles. However future explorations could consider spiral structure consistent with Swing amplification (e.g., Fuchs 2001). Here we have focused on stars initially on circular orbits, however future explorations could consider stars born in spiral arms. Whereas in this paper we used a test-particle approach as was done by De Simone et al. (2004), future explorations can aim to produce self-consistent models where the orbits of the stars are consistent with the spiral density waves themselves.

We wish to thank Gunnar Paesold for useful discussions and for his close assistance in software development. We also thank E. Blackman and A. Hubbard for helpful comments. Support for this work was in part provided by National Science Foundation grant ASST-0406823, and the National Aeronautics and Space Administration under Grant No. NNG04GM12G issued through the Origins of Solar Systems Program.

REFERENCES

- Binney, J., & Tremaine, S. 1987, *Galactic Dynamics*, Princeton University Press, Princeton, NJ
- Carlberg, R. G., & Sellwood, J. A. 1985, *ApJ*, 292, 79
- Carr, B. J., & Lacey, C. G. 1987, *ApJ*, 316, 23
- Combes, F., Debbasch, F., Friedli, D., & Pfenniger, D. 1990, *A&A*, 233, 82
- Contopoulos, G. 1981, *A&A*, 102, 265
- Contopoulos, G. 1985, *Comments on Astrophysics, Physics*, 11, 1
- Contopoulos, G., & Grosbol, P. 1988, *A&A*, 155, 11
- Dehnen, W. 1998, *AJ*, 115, 2384
- Dennis, T. R. 1966, *ApJ*, 146, 581
- De Simone, R. S., Wu, X., & Tremaine, S. 2004, *MNRAS*, 350, 627
- Dias, W. S. & J. R. D. Lpine, J. R. D. 2005, *astro.ph*, 3083
- Drimmel, R., & Spergel, D.N. 2001, *ApJ*, 556, 181
- Eggen, O. J., Lynden-Bell, D., & Sandage, A. R. 1962, *ApJ*, 136, 748
- Elmegreen, B. G., Elmegreen, D. M., & Montenegro, L. 1992, *ApJS*, 79, 37
- Fuchs, B. 2001, *A&A*, 368, 107
- Fux, R. 2001, *A&A* 373, 511
- Hänninen, J., & Flynn, C. 2002, *MNRAS*, 337, 731
- Hänninen, J., & Flynn, C. 2004, *A&A*, 421, 1001
- Henry, A. L., Quillen, A. C., & Gutermuth, R. 2003, *AJ*, 126, 2831
- Jenkins, A., & Binney, J. 1990, *MNRAS*, 245, 305
- Jenkins, A. 1992, *MNRAS*, 257, 620
- Lacey, C. G. 1984, *MNRAS*, 208, 687
- Lacey, C. G., & Ostriker, J. P. 1985, *ApJ*, 299, 633
- Lecar, M., Franklin, F., Holman, M., Murray, N. 2001, *ARA&A*, 39, 581
- Lepine, J. R. D., Mishurov, Y. N., & Dedikov, S. Y. 2001, *ApJ*, 546, 234
- Lin, C. C., Yuan, C., Shu, & Frank H. 1969, *ApJ*, 155, 721
- Lowe, S. A., Roberts, W. W., Yang, J., Bertin, G., & Lin, C. C. 1994, *ApJ*, 427, 184
- Lynden-Bell D., & Kalnajs A. J. 1972, *MNRAS*, 157, 1
- Ma, J., Zhao J., Zhang F., & Peng Q. 2000, *ChA & A*, 24, 435
- Mihalas, D., & Binney, J. J. 1981, *Galactic Astronomy*, Freeman: San Francisco
- Murray, N., & Holman, M. 1999, *Science*, 283, 1877
- Naoz, S., & Shaviv, N. 2005, *ApJ*, in press, (astro-ph/0503127)
- Quillen, A. C. 2003, *AJ*, 125, 785
- Quillen, A. C. & Minchev, I. 2005, *AJ*, 130, 576
- Rix, H. W., & Rieke, M. J. 1993, *ApJ*, 418, 123
- Sellwood, J. A., & Carlberg, R. G. 1984, *ApJ*, 282, 61
- Sellwood, J. A., & Binney, J. J. 2002, *MNRAS*, 336, 785
- Spitzer, L. & Schwarzschild, M. 1951, *ApJ*, 114, 385
- Spitzer, L. & Schwarzschild, M. 1953, *ApJ*, 118, 106
- Toomre, A. 1981 in S.M. Fall, D. Lynden-Bell (eds.), *The Structure and Evolution of Normal Galaxies*, Cambridge Univ. Press, Cambridge, p. 111
- Vallée, J. 2005, *AJ*, 130, 569
- Velazquez, H., White, S. 1999, *MNRAS*, 304, 254
- Wielen, R. 1977, *A&A*, 60, 263

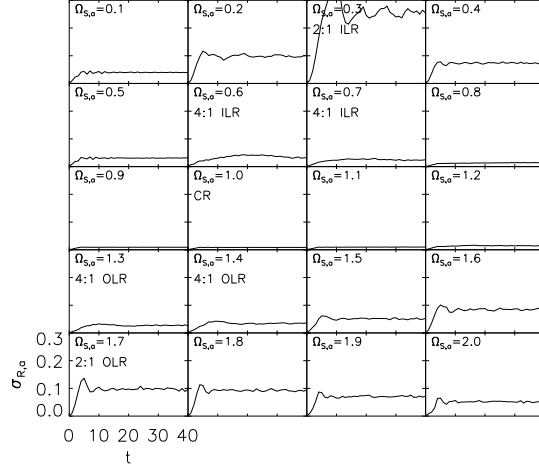


FIG. 1.— Radial velocity dispersion as a function of time for the primary 2-armed spiral pattern only. Each panel shows a different value of the angular velocity $\Omega_{s,a}$. The gravitational potential amplitudes are $\epsilon_a = -0.006$ and $\epsilon_b = 0$. The 2:1 Inner Lindblad Resonance (ILR) and Outer Lindblad Resonance (OLR) occur at $\Omega_{s,a} = 0.3\Omega_0$ and $\Omega_{s,a} = 1.7\Omega_0$ respectively. Time is in units of rotational periods and the radial velocity dispersion σ_R is in units of the circular velocity V_0 . Note the low values of σ_R around the corotation radius $\Omega_{s,a} = 1.0$. There is no increase in σ_R once the wave is grown.

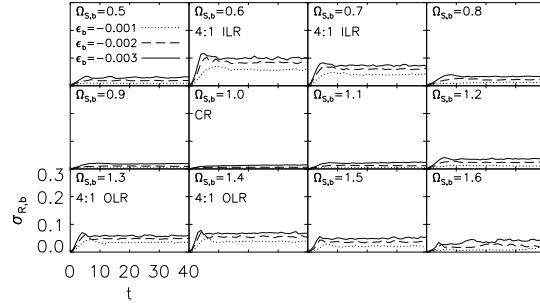


FIG. 2.— Radial velocity dispersion as a function of time for the secondary, 4-armed spiral pattern only. Each panel shows a different value of the angular velocity $\Omega_{s,b}$. The 4:1 Inner Lindblad Resonance (ILR) and Outer Lindblad Resonance (OLR) occur at $\Omega_{s,b} = 0.35, 1.65$, respectively. Since we incremented $\Omega_{s,b}$ by 0.1 this figure does not show a panel exactly at OLR or ILR. Thus we labeled the LRs on each side of their occurrence. Different line styles show different values of the spiral wave gravitational potential perturbation: $\epsilon_b = -0.001$ (dotted), $\epsilon_b = -0.002$ (dashed), and $\epsilon_b = -0.003$ (solid).

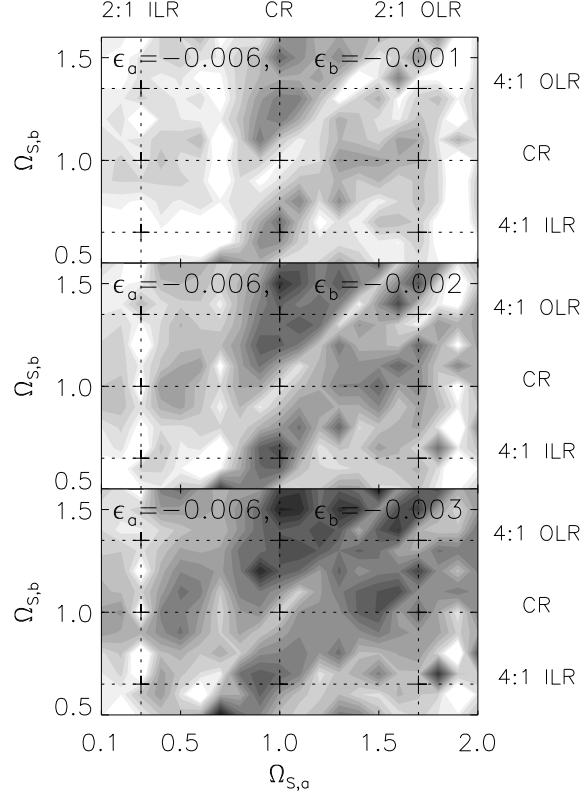


FIG. 3.— Contours show $\Delta\sigma_R \equiv \sigma_{R,ab} - \sqrt{\sigma_{R,a}^2 + \sigma_{R,b}^2}$ for 3 values of the amplitude of the secondary spiral wave, $\epsilon_b = -0.001, -0.002, -0.003$, and a constant value of the primary amplitude, $\epsilon_a = -0.006$ in $(\Omega_{s,a}, \Omega_{s,b})$ -space. Spiral amplitudes were grown simultaneously in 4 periods and were kept fixed after that. Here $\sigma_{R,a}$ and $\sigma_{R,b}$ are the radial velocity dispersions as a result of only the primary or only the secondary spiral patterns, respectively. These were time averaged over 40 galactic rotations, excluding the time during which wave amplitudes grew (4 rotation periods). Similarly, $\sigma_{R,ab}$ is the time average of a simulation run with both patterns perturbing the test particles. Consequently, $\Delta\sigma_R$ gives the additional heating caused by the combined effect of the two perturbers as opposed to the sum of the heating that would have been produced if each spiral wave propagated alone. In all panels $\Delta\sigma_R$ was normalized to its maximum value in the three panels allowing a proper comparison among the panels. The pattern speed of the primary wave, $\Omega_{s,a}$, varies between 0.1 and 2.0 and that of the secondary one, $\Omega_{s,b}$, varies between 0.5 and 1.6 in units of the angular rotation rate, $\Omega_0 = 1$ at $R_0 = 1$. The dashed lines show the locations of corotation and Lindblad resonances due to each of the two spiral wave perturbations. Next to each dashed line we labeled the resonances by denoting the corotation resonance with "CR", and the outer and inner Lindblad resonances by "OLR" and "ILR". For a given set of pattern speeds, a line at 45° slope predicts the variation of $\Delta\sigma_R$ with radius, R , where the intercept of the line is set by the relative angular frequency, $\Delta\Omega_s \equiv \Omega_{s,a} - \Omega_{s,b}$. Large values of $\Delta\sigma_R$ are primarily observed along the lines $\Omega_{s,a} = 1.0$ and $\Omega_{s,b} = 1.0$, which correspond to the CR of each pattern, with the exception of the intersection of these lines; $\Delta\sigma_R(R)$ is a strong function of radius.

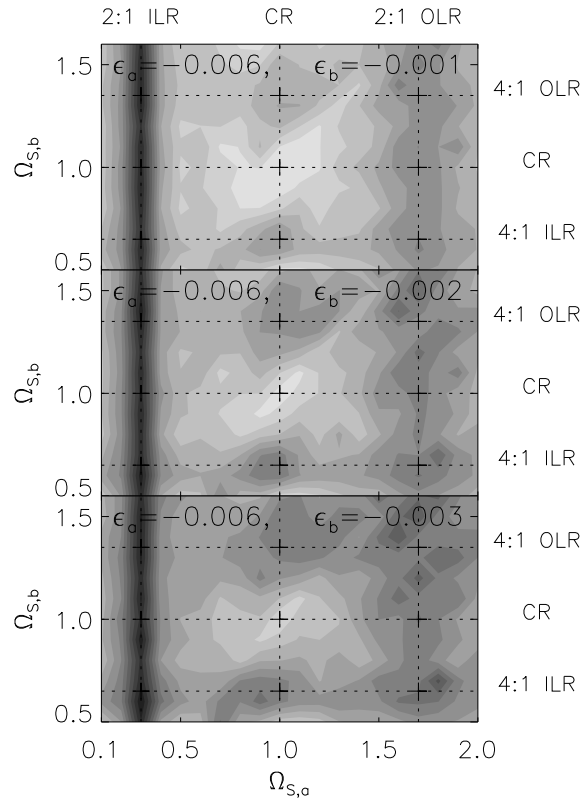


FIG. 4.— Contour plots of the heating produced by the propagation of 2 spiral waves. Identical setup as in Fig. 3 but contours show $\sigma_{R,ab}$, instead of $\Delta\sigma_R$. Aside from the 2:1 LRs of the primary, 2-armed spiral wave, maximum values of $\sigma_{R,ab}$ are found at and around the CR with the primary and 4:1 LRs of the secondary patterns. As in Fig. 3, at the CR with both spiral waves very low radial velocity dispersion is seen (here it is a minimum). For all panels $\sigma_{R,ab}$ was normalized to the largest value in the figure.

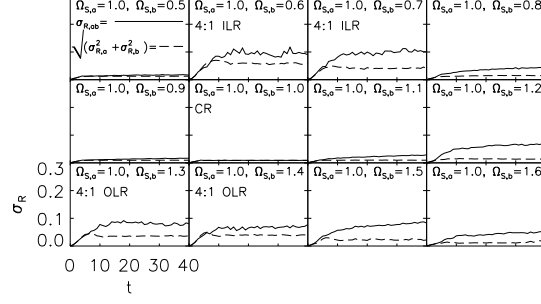


FIG. 5.— Time evolution of the radial velocity dispersion, $\sigma_{R,ab}$, as a result of the simultaneous propagation of a 2- and a 4-armed spiral patterns (solid line). Time is in units of galactic rotations. The 2-armed spiral structure has the same parameters as the panel in Fig.1 for which $\Omega_{s,a} = 1.0$ (CR), whereas the 4-armed spiral wave has different angular velocity in each panel. The time evolution of the radial velocity dispersion due to the latter perturbation alone, $\sigma_{R,b}$, was shown in Fig. 2. For comparison, in addition to $\sigma_{R,ab}$ (solid line) we also plotted $\sqrt{\sigma_{R,a}^2 + \sigma_{R,b}^2}$ (dashed line) (see Eq. 10). The values of the perturbation amplitudes are $\epsilon_a = -0.006$ and $\epsilon_b = -0.001$. We note the following dynamical effects around the 4:1 ILR and OLR in the case of $\sigma_{R,ab}$: (1) $\sigma_{R,ab}$ increases up to a factor of ≈ 3 compared to the dispersion expected from the noninteracting spiral waves, $\sqrt{\sigma_{R,a}^2 + \sigma_{R,b}^2}$; (2) $\sigma_{R,ab}$ grows with time; (3) resonances have effect over a larger range of angular velocities, compared to $\sqrt{\sigma_{R,a}^2 + \sigma_{R,b}^2}$, and thus over a larger range of radii.

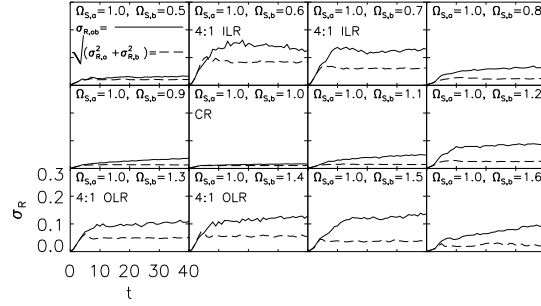


FIG. 6.— Same as Fig.5 but with the secondary gravitational potential amplitude $\epsilon_b = -0.002$. The radial velocity dispersion at the LR saturates faster than that in Fig. 5 as $|\epsilon_b|$ was increased from 0.001 to 0.002.

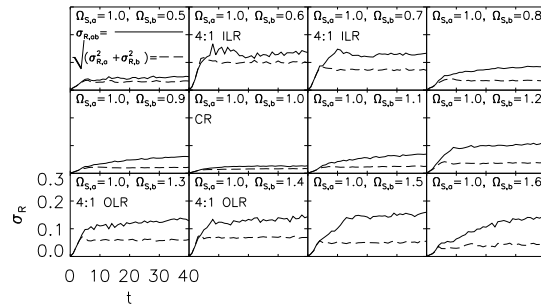


FIG. 7.— Same as Figures 5 and 6 but with the secondary gravitational potential amplitude $\epsilon_b = -0.003$. Note the further decrease in the saturation time of $\sigma_{R,ab}$ as compared to Figures 5 and 6.

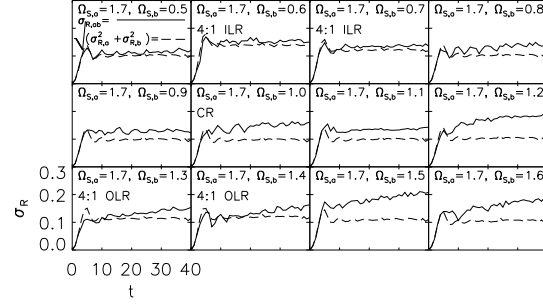


FIG. 8.— Same as Figure 7 but with the primary spiral wave placing test particles at the 2:1 OLR ($\Omega_{s,a} = 1.7$), instead of the CR. As in Figures 5-7, both spirals were grown simultaneously in the initial 4 rotation periods; the perturbation amplitudes are $\epsilon_a = -0.006$ and $\epsilon_b = -0.003$.

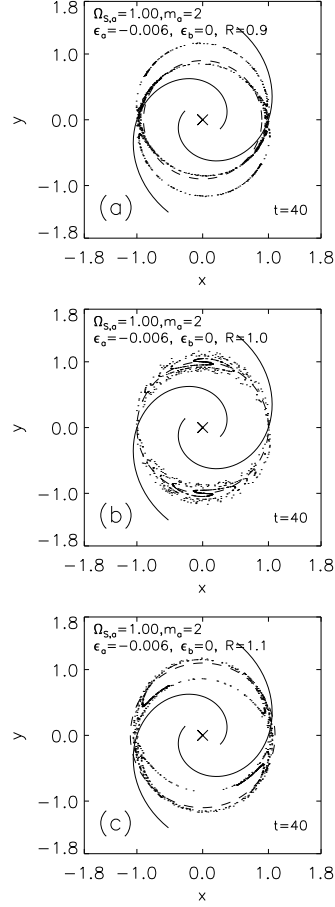


FIG. 9.— A snapshot of the evolution of a ring of stars subjected to a 2-armed spiral perturbation grown in the initial 4 rotation periods. The time is $t = 40$ rotations. The pattern speed is the same for each panel, $\Omega_{s,a} = 1.0$, but the radius of the initial real-space particle distribution varies as: (a) $R = 0.9$, which places stars just inside the CR; (b) $R = 1.0$, placing stars exactly at the CR; and (c) $R = 1.1$, placing stars just outside the CR. The initial ring in each panel is indicated by the dashed line. The parameter α_a has the default value of -6 which corresponds to a pitch angle $p_a \simeq -18^\circ$. The curves on which stars lie formed at time $t \approx 4$ rotation periods and remained fixed in the reference frame of the spiral structure for the rest of the run.

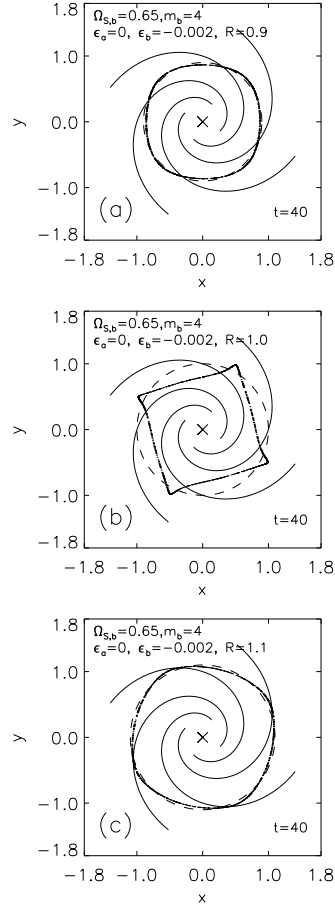


FIG. 10.— A snapshot of the evolution of a ring of stars subjected to a 4-armed spiral wave at and near the 4:1 ILR. The time is $t = 40$ rotations as in Fig. 9. The pattern speed is the same for each panel, $\Omega_{s,b} = 0.65$, but the radius of the initial real-space particle distribution varies as: (a) $R = 0.9$, which places stars just inside the 4:1 ILR; (b) $R = 1.0$, placing stars exactly at the 4:1 ILR; and (c) $R = 1.1$, placing stars just outside the 4:1 ILR. The initial ring in each panel is indicated by the dashed line. The parameter $\alpha_b = -12$, corresponding to a pitch angle $p_b \simeq -18^\circ$. The curves on which stars lie for $R = 0.9, 1.1$ were approximately constant in shape and orientation with time, as viewed in the rotation frame with the spiral wave. In contrast, exactly at the 4:1 ILR the rectangular curve spins clockwise with a period of about 9 rotations.

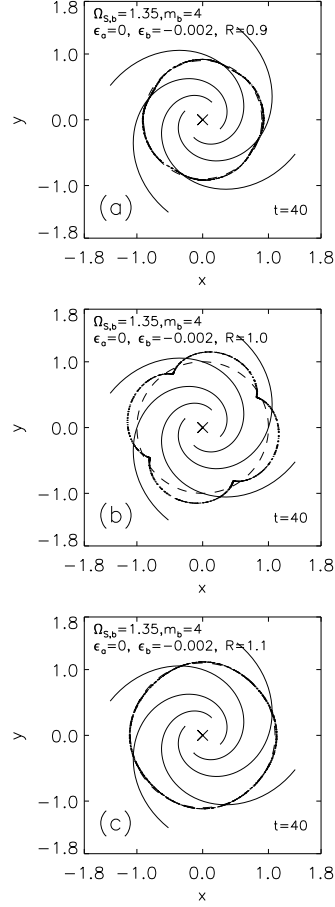


FIG. 11.— Same as Fig. 10 but with the angular velocity of the secondary pattern $\Omega_{s,b} = 1.35$, which places stars at the 4:1 OLR at $R = R_0$. The pattern speed is the same for each panel, $\Omega_{s,a} = 0.65$. As in Fig. 10, only when the initial particle distribution placed stars exactly at the resonance, panel (b), did the curve on which stars lie change shape and orientation with time.

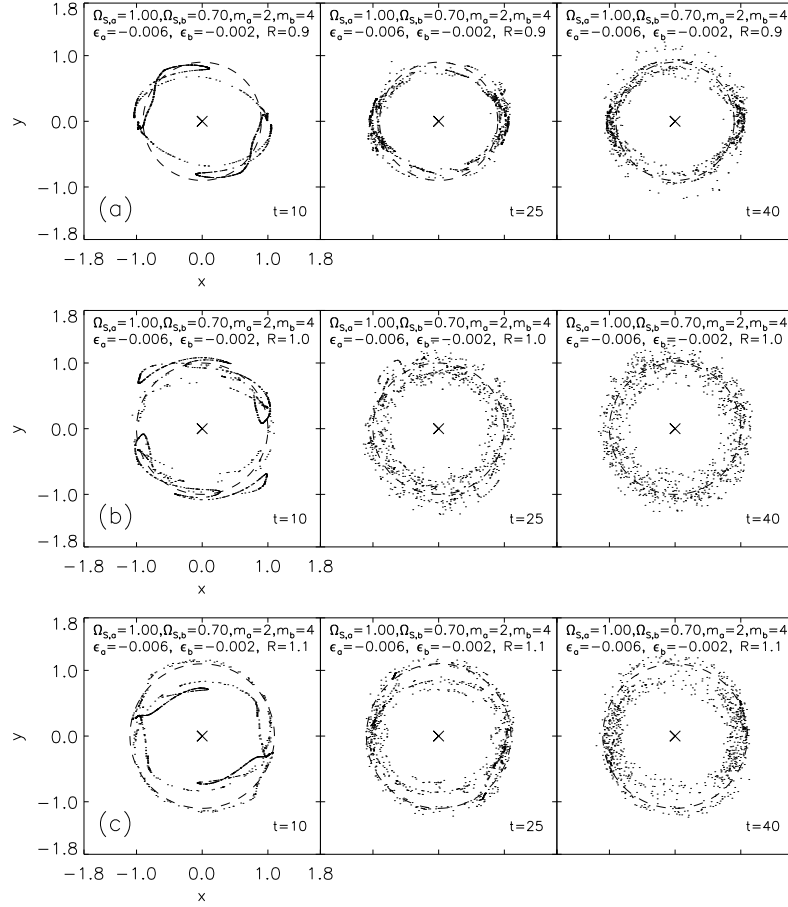


FIG. 12.— Snapshots of the 3-step time evolution of 3 rings of stars subjected to both a 2-armed spiral wave near the CR and a 4-armed one near the 4:1 ILR. This corresponds to the panel with $\Omega_{s,b} = 0.7$ in Fig. 6. Time develops in each row from left to right. Note the very different morphology compared to Figures 9-11. Stars are observed to diffuse radially. All parameters of the primary spiral wave in each row are the same as those used in each row in Fig. 9. The difference here is that a second spiral wave is propagating in addition to the primary one and that we plot 3 steps of the time evolution since changes are taking place unlike in the time evolution of the systems shown in Fig. 9. Rows from top to bottom show particles subjected to 2 spiral wave perturbations moving at pattern speeds of $\Omega_{s,a} = 1.0$ and $\Omega_{s,b} = 0.7$ and initially positioned in a ring of radius: (a) $R = 0.9$, (b) $R = 1.0$, and (c) $R = 1.1$. Snapshots are at times $t = 10, 25, 40$. The dashed circles show where stars were positioned initially with a uniform azimuthal distribution. The crosses show the position of the galactic center.

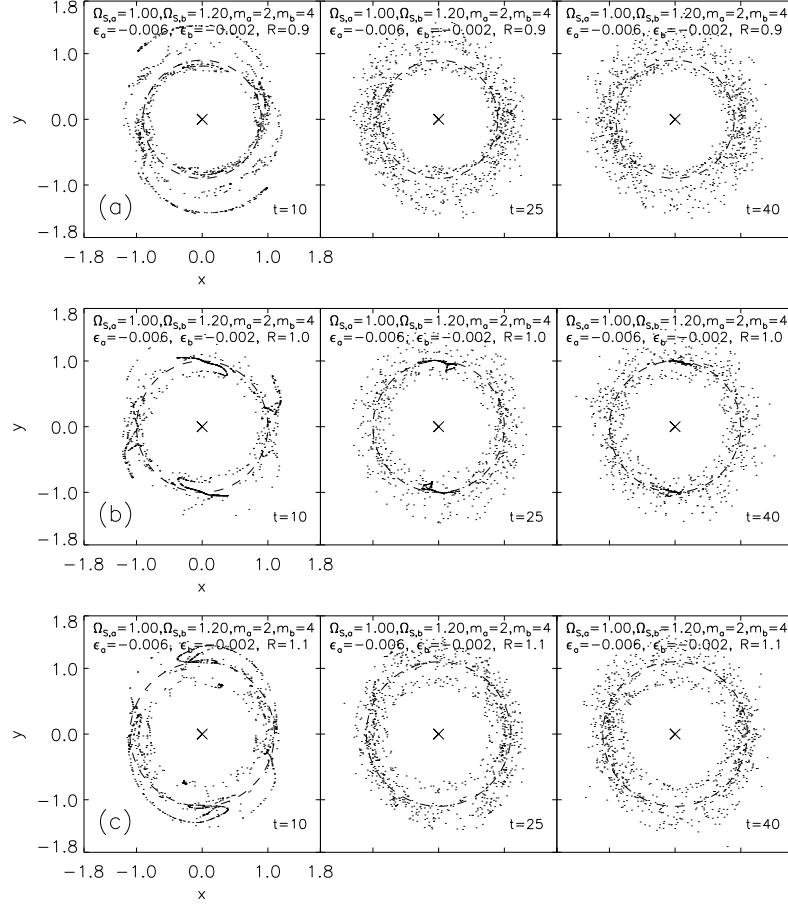


FIG. 13.— Same as Fig. 12 but with the secondary pattern speed near the 4:1 OLR, $\Omega_{s,b} = 1.2$. This corresponds to the panel with $\Omega_{s,b} = 1.2$ in Fig. 6. The radial diffusion of stars is notably increased compared to Fig. 12.

TABLE 1
PARAMETERS DESCRIBING SIMULATIONS

Figures	ϵ_a	ϵ_b	α_a	α_b	m_a	m_b	$\Omega_{s,a}$	$\Omega_{s,b}$
1	-0.006		-6		2		0.1,0.2,...,1.9,2.0	
2		-0.001,-0.002,-0.003		-12		4		0.5,0.6,...,1.5,1.6
3,4	-0.006	-0.001,-0.002,-0.003	-6	-12	2	4	0.1,0.2,...,1.9,2.0	0.5,0.6,...,1.5,1.6
5	-0.006	-0.001	-6	-12	2	4	1.0	0.5,0.6,...,1.5,1.6
6	-0.006	-0.002	-6	-12	2	4	1.0	0.5,0.6,...,1.5,1.6
7	-0.006	-0.003	-6	-12	2	4	1.0	0.5,0.6,...,1.5,1.6
8	-0.006	-0.003	-6	-12	2	4	1.7	0.5,0.6,...,1.5,1.6
9	-0.006		-6		2		1.0	
10		-0.002		-12		4		0.65
11		-0.002		-12		4		1.35
12	-0.006	-0.002	-6	-12	2	4	1.0	0.7
13	-0.006	-0.002	-6	-12	2	4	1.0	1.2

NOTE. — Spiral pattern parameters corresponding to simulations shown in the Figures. The perturbation strengths ϵ_1 and ϵ_2 are given in units of V_0^2 , the velocity of a star in a circular orbit at R_0 . The pattern speeds, $\Omega_{s,a}$ and $\Omega_{s,b}$, are in units of $\Omega_0 = V_0/R_0$. The parameters α_a and α_b set the pitch angles of the spiral arms as $m_a \cot(p_a) = \alpha_a$ and identically for m_b, p_b, α_b , where p_a and p_b are the pitch angles of the 2-armed and 4-armed spirals, respectively. Two different initial spatial distributions were used: (1) a uniform distribution in both R and ϕ in the annulus $(R_0 - \Delta R, R_0 + \Delta R)$ with $\Delta R = 0.3$ (Figures 1-8); (2) a uniform distribution in the azimuthal direction and a delta peak at $R = R_0$, i.e., a ring of stars at $R = R_0$ (Figures 9-12)